Chapter 3

Soft-Templated Synthesis of Manganese Oxides and their Catalytic Applications

3.1. Soft-Templated Synthesis of Mn₃O₄ Microdendelions for Photocatalytic Dye Degradation

3.1.1. Introduction

In recent years, the fabrication of metal oxide superstructures has fascinated scientists for studying the physics of materials in two- or three-dimensions and their potential technological applications.[1-3] Self-organisation of metal oxide nanostructures provides extraordinary richness of morphological and physicochemical diversity for emerging unprecedented architectures.[4-6] Manganese oxides are materials of considerable importance due to their interesting structural, electronic and magnetic properties that arise from their outstanding structural flexibility combined with novel physical and chemical properties.[7,8] Moreover, manganese oxides are ubiquitous in nature and environmental friendly that deserve their applications in catalysis, renewable energy, and environmental remediation.[9,10] Among the series of manganese oxides available in various oxidation states of manganese (II, III, IV), Mn_3O_4 (hausmannite) has been found to be an effective and inexpensive catalyst in versatile reactions.[11-17] The corresponding surface energy values of Mn_3O_4 (0.96 ± 0.08 J m^{-2}), Mn_2O_3 (1.29 ± 0.10 J m^{-2}), and MnO_2 (1.64 ± 0.10 J m^{-2}), suggest considerable thermodynamic stability of Mn_3O_4 over other oxidation states.[18] Moreover, Mn_3O_4 possess several special structural attributes[19]: (i) it shows semicovalent character in tetrahedral sites (Mn II occupancy with Mn–O distance of 1.812 Å) and in the apical bonds of octahedral sites (Mn III occupancy with Mn–O lengths of 2.386 Å); (ii) the remaining bonds of the octahedra display ionic character with a Mn–O length of 2.977 Å; and (iii) the observed distortion in the octahedra found in both phases can be explained by a Jahn–Teller effect due to the d^4 state of the Mn III atoms in high spin configuration. Bulk Mn_3O_4 is a *p*-type semiconductor with a wide direct band gap of 2.3 eV and is the stablest among all the manganese oxides possessing tetragonally distorted spinel structure.[20]

The removal of the non-biodegradable organic chemicals is a global ecological problem. Dyes are an important class of synthetic organic compounds which are commonly used in textile industries and therefore, are common industrial pollutants. However, due to the inherent stability of modern dyes, conventional biological treatment methods for industrial waste water are ineffective. Photocatalysis, where photons are used for catalytically activating chemical reactions on the surface of

photosensitized catalysts, remains one of the leading hubs of research for harvesting the solar light.[21-23] The efficiency of a photocatalytic process, mostly, depends on the nature of photosensitized catalyst, suitable photon source for excitation, the substrate which can rapidly accept the photogenerated charge carriers and the spatial distance between the catalyst and substrate.[24] Typically, photocatalysts generate the charge carriers on excitation and under suitable conditions, these are transferred from the catalysts to the reaction medium, which in turn initiate the chemical reaction.[25] Since the pioneering work of Fujishima and Honda in 1972, photocatalysis by semiconductor metal oxide. Alizarin red, an industrially important synthetic textile dye of anthraquinone family, is a widespread polluting dye, whose inexpensive and environmental friendly elimination from effluents is a serious challenge. Although, the chemical and electrochemical degradation of alizarin red have been carried out by immobilized 5,10,15,20-tetrakis(4-sulfonatophenyl)porphine-Mn(III) as a biomimetic peroxidase-like catalyst,[27] electro-Fenton process using a graphite-felt cathode,[28] hybrid gas-liquid dielectric barrier discharge,[29] the photochemical degradation of the dye has, mainly, be relied upon the advent of semiconductor nanocatalysts. While the visible light-driven photocatalytic degradation of alizarin red has been carried out using nanostructures of TiO_2,[30] Bi-doped TiO_2,[31] ZnO,[32] Ag-impregnated ZnO,[33] CdS,[34] TiO_2-In_2O_3 composites,[35] UV-light assisted degradation has been pursued by TiO_2,[36] nanometer TiO_2 film,[37] electrospun bismuth oxoiodide nano/microtectonic plate-like structures[38] etc. In addition, sonophotocatalytic degradation of the dye has also been experimented with TiO_2 nanostructures.[39] Therefore, it is revealed that the photocatalytic degradation of alizarin red has, mostly, been experimented with TiO_2 or ZnO nanostructures or their composites. Based on these perspectives, Mn_3O_4, bearing many special structural attributes[19,40] and with the possibility of designing high surface area hierarchical 3D nano/microstructures[41] could offer an alternative low-cost, earth abundant, semiconductor, heterovalent-Mn photocatalyst for the degradation of alizarin red under visible light illumination. Moreover, during the past decade, much attention has been paid to investigations into the photocatalytic degradation of organic pollutants with metal oxide particles under UV light radiation.[48] Based on these perspectives, the synthesis of high surface area Mn_3O_4 superstructures and their application as photocatalysts could be investigated.

Several synthetic strategies have been adopted, so far, in the literature for the fabrication of size and shape-selective manganese oxide nanocrystals and their

assemblies using different types of soft templates and their application in catalysis. Chen and group[42] have described the synthesis of octahedral Mn_3O_4 nanocrystals by soft-template of cetyltrimethylammoniumbromide/poly(N-vinyl 2-pyrrolidone) mixture and the crystallites have been found to act efficient catalysts for the degradation of methylene blue. Ahmed and co-workers[43] have reported the synthesis of nanosized Mn_3O_4 single crystals using polyol method and investigated their catalytic activity towards the decomposition of aqueous hydrogen peroxide and degradation of methylene blue at room temperature. Takada and colleagues[44] have illustrated microorganism-mediated synthesis of nano- and micro-architectural manganese oxides that catalyse the selective bromination of hydrocarbons under irradiation of fluorescent light. Huang and co-authors[45] have reported the synthesis of Mn_3O_4 nanoparticles and hexagonal nanoplates by a solvothermal oxidation process and these materials were found to be catalytically active towards oxidation of aldehydes. Hu and co-workers[46] have described the synthesis of well-dispersed ultrafine Mn_3O_4 nanoparticles on graphene, which act as promising catalysts for one-step thermal decomposition of ammonium perchlorate at a fairly reduced temperature. Yitai group[47] have described hydrothermal process for the synthesis of branched mesoporous Mn_3O_4 nanorods by using potassium permanganate and poly(ethylene glycol) as starting materials. It was noted that the mesoporous nanorods are efficient catalysts for the degradation of methylene blue inthe presence of H_2O_2 at 80 °C. It is, therefore, apparent that copious amount of reports on the synthesis and to study the catalytic activity of Mn_3O_4 particles are limited at the nanoscale.

In this sub-section, we have described the synthesis of dandelion shaped Mn_3O_4 microstructures using dye/surfactant assemblies as soft-templates. The assemblies so formed have been characterised by absorption spectroscopy, FTIR, HRTEM, SEM, EDX, SAED, XRD and TGA analysis. The surface area of the particles has been measured by BET analysis. The catalytic activity of the particles has been screened by studying the photocatalytic degradation of an aqueous solution of alizarin red under visible light illumination.

3.1.2. Experimental

3.1.2.1. Synthesis of Mn_3O_4 Microdandelions using Dye-Surfactant Composites

The superstructures of manganese oxide have been synthesised using dye-surfactant conjugates in a particular molar ratio and manganese acetate tetrahydrate as the precursor salt. In a typical synthesis, an aliquot of aqueous FITC-D 2000S (0.5 nM) was

added to an aqueous solution of CTAB (10 μM) in double-necked round-bottom flask so that the total volume of the solution is 25 mL and the mixture was stirred overnight at room temperature. Now, an amount of 0.245 g $Mn(ac)_2.4H_2O$ was dissolved in the dye-surfactant mixture by refluxing on a water bath at 65°C. After complete dissolution of the precursor, 100 μL diethanolamine was added and refluxing was continued for another 6 h. After about 30 min, the reaction mixture, suddenly, turned into yellowish brown from a colourless solution indicating the formation of manganese oxide superstructures. As the refluxing was continued, the colour slowly changed into deep brown pointing out to the aggregation between the ultrasmall manganese oxide particles. Then, the water bath was removed and the reaction mixture was stirred for 12 h at room temperature. The particles formed by this method was washed five times with slightly hot water and finally, dispersed in water. The manganese oxide nanoparticles prepared by this method are stable for a month and can be stored in the desiccator for several days without any significant agglomeration or precipitation of the particles.

3.1.2.2. Photocatalytic Reaction

The photocatalytic activity of Mn_3O_4 microdandelions was tested by following the degradation of an organic dye, alizarin red in aqueous solution. The as-synthesised Mn_3O_4 microdandelions was annealed at 500 ˚C in argon atmosphere for 1 h to remove the organics so as to avoid any influence of the FITC-D 2000S or CTAB in the catalytic reaction. In the photocatalytic experiments, 25 μg of the dried catalysts was dispersed with 3.0 ml of 2.0 μM aqueous solution of the dye and the solution was stirred in the dark for 2 h to reach adsorption-desorption equilibrium between the catalysts and alizarin red. Then, the mixture was irradiated by a 60 W tungsten lamp and the progress of the reaction was followed in the absorption spectrophotometer.

3.1.3. Results and Discussion

3.1.3.1. Absorption Spectroscopy

The absorption spectral features of the Mn_3O_4 particles in the solid state are shown in Fig. 3.1. The dye or the surfactant molecules do not exhibit any characteristic absorption spectral features in the prescribed low concentration (1.0 nM) employed for this experiment although FITC in aqueous medium shows a sharp absorption maximum at 289 nm and a broad absorption band with maximum at 490 nm at a certain higher concentration range.[49] The electronic absorption spectrum of assemblies shows three well-defined regions: the first portion from 220 to 300 nm, the second from 310 to 500 nm (with a maximum at 325 nm), and the third one finishing at 800 nm. The first portion is attributed to charge transfer transitions, and the last two can be, reasonably, related to d-d crystal field transitions, $^3E_g(G) \leftarrow {}^3T_{1g}$, $^3A_{2g}(F) \leftarrow {}^3T_{1g}$, $^3A_{2g}(G) \leftarrow {}^3T_{1g}$, $^3T_{2g}(H) \leftarrow {}^3T_{1g}$, $^3T_{1g}(H) \leftarrow {}^3T_{1g}$ and $^3E_g(H) \leftarrow {}^3T_{1g}$, on octahedral Mn^{3+} species corresponding to manganese oxide particles in the superstructures.[50] The appearance of a strong peak at around 325 nm is due to the allowed $O^{2-} \rightarrow Mn^{2+}$ and $O^{2-} \rightarrow Mn^{3+}$ charge transfer transitions.[51] These results indicate that manganese oxide particles are embedded in the dye or surfactant or dye-surfactant hybrid assemblies. The direct band gap energy (E_g) for the manganese oxide superstructures could be determined by fitting the absorption data to the direct band gap transition equation as,[52] $(\alpha h\nu)^2 = A(h\nu - E_g)$, where, α is the absorption co-efficient, $h\nu$ the photon energy and A a constant. The absorption coefficient (α) is defined as: $\alpha = 2.303$ A/L c, where, A is the absorbance of the sample, c the loading of sample (g L^{-1}), L the path length (= 1 cm). Profile showing a plot of $(\alpha h\nu)^2$ as a function of $h\nu$ is shown in panel b and the extrapolation of linear portions of the curve towards absorption equal to zero offers a measure of the
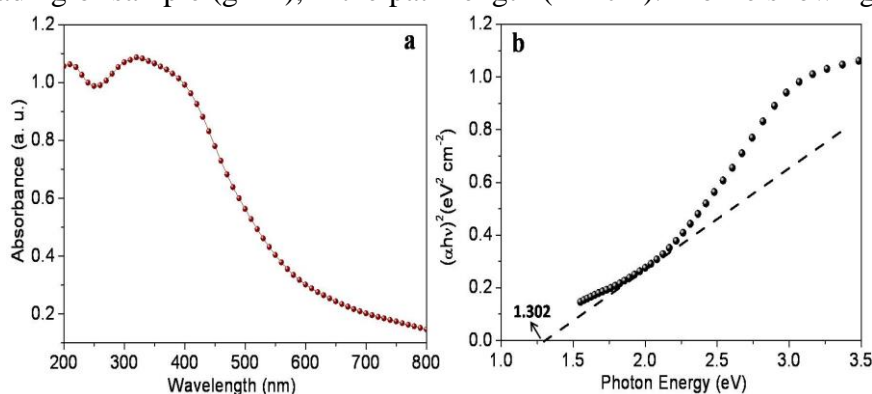

Fig. 3.1. (a)Solid state absorption spectrum and (b) plot of $(\alpha h\nu)^2$ as a function photon energy of Mn_3O_4 microdandelions in dye-surfactant conjugates.

direct band gap transitions, E_g. The estimated direct band gap of the Mn_3O_4 was found to be 1.302 eV; this value is considerably different from the reported value of bulk

Mn_3O_4.[20] The conjugation of FITC-D2000S/CTAB through effective intermolecular complexation between complementary binding sites on dye and surfactant molecules and the presence of manganese precursor led to synergistic effect in the formation of superstructures.[49]

3.1.3.2. Morphology, Composition and Crystallinity of the Microdendelions

The morphology, composition and crystallinity of the as-prepared Mn_3O_4 assemblies synthesised at the dye-surfactant conjugates are described in Fig. 3.2. Low resolution scanning electron micrograph (panel a) shows Mn_3O_4 nanobuilding units are self-assembled into micrometer-sized aggregates with dandelion-like appearances. Inset shows the photograph of a real dandelion showing the morphological resemblance with the particles. At a relatively higher resolution (panel b), flower-like arrangements with average diameters *ca.* 1.0 µm is seen. At higher resolution (panel c), petals of the flowers are apparent that
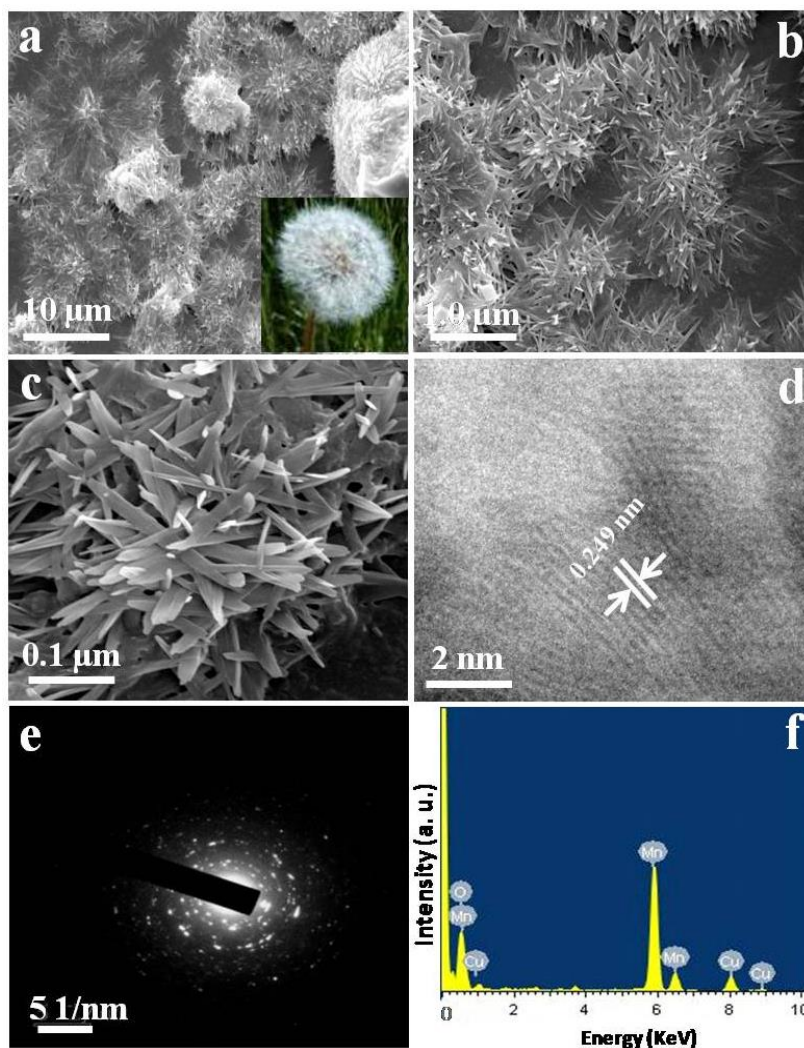

Fig. 3.2. (a-c) Scanning electron microscopic images of Mn_3O_4 microdendelions in dye-surfactant assemblies; (d) high resolution TEM, (e) selected area electron diffraction, and (f) electron diffraction X-ray spectrum. Inset in panel a shows the photograph of real dandelions to show the resemblance with the Mn_3O_4 microstructures.

demonstrate adequate stabilisation of the nanoparticles with a high degree of organisational selectivity.[53]High resolution TEM image (panel d) of Mn_3O_4 microdandelions displays the interplanar distance between the fringes is about 0.249

nmwhich corresponds to the distance between the (211) planes of the Mn_3O_4 tetragonal crystal lattice.Selected area electron diffraction pattern (panel e) of the Mn3O4 particles is consistent with tetragonal Mn3O4 with strong ring patternsdue to (101), (103) and (220) planes and therefore, confirms the crystallinity of the particles.[54] Representative energy dispersive X-ray spectrum (panel f) of Mn_3O_4 particles of dye-surfactant/manganese oxide hybrid assemblies reveals that the particles are composed of Mn, O, C elements. The signals of C, O and Cu elements come from the stabilizer dye, surfactant and the supporting TEM grid.

3.1.3.3. Fourier Transform Infrared Spectroscopy

The formation of manganese oxide particles in the dye-surfactant conjugates have been seen through FTIR spectroscopy. Fig. 3.3 shows a comparison of the FTIR spectra for pure FITC-D 2000S/CTAB conjugates and the composite dye-surfactant/manganese oxide superstructures.In trace a, the FTIR spectrum of dye-surfactant conjugates shows the characteristic –N=C=S peak located at the region of 2333–2359 cm^{-1} along withthe presence of aromatic –OH at 3163 cm^{-1} and the ether linkage at 1105 cm^{-1} corresponding to
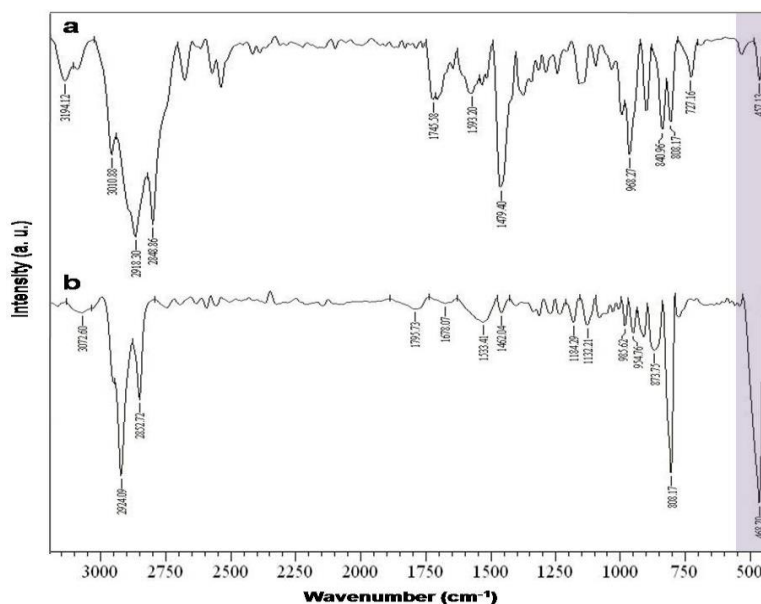

Fig. 3.3. FTIR spectra of (a) FITC-D 2000S/CTAB and (b) after formation of Mn_3O_4 microdendelions in FITC-D 2000S/CTAB soft template at room temperature.

FITC-D 2000S, and C–N stretch at 1207 cm^{-1}corresponding to CTAB are seen.[49] It is observed that, in the conjugates, the intensities for nearly all of the vibrations are weakened and furthermore, several vibrations are missing, pointing out to the complexation between dye and surfactant molecules. In trace b, the band at 457 cm^{-1}, which is marked with a shadowed area, is the characteristic stretch of Mn–O indicatingthe formation of manganese oxide in the superstructures. The twoabsorption bands located at 2924 and 2852 cm^{-1} could be assigned to the symmetric and

asymmetric stretching modes of the –CH$_2$ groups of the CTAB surfactant bound to the surface of Mn$_3$O$_4$, respectively.[55]

3.1.3.4. X-ray Diffraction Pattern

The X-ray diffraction pattern of the Mn$_3$O$_4$ microdandelions is shown in Fig. 3.4. Trace a is of the manganese oxide/dye-surfactant hybrid assemblies; all diffraction peaks implying a crystalline structure can be indexed to the tetragonal hausmannite structure with lattice parameters, a = b = 5.762 Å, and c = 9.469 Å and space group $I4_{I/amd}$, which are consistent with the standard values of bulk Mn$_3$O$_4$ (JCPDS# 24-0734).
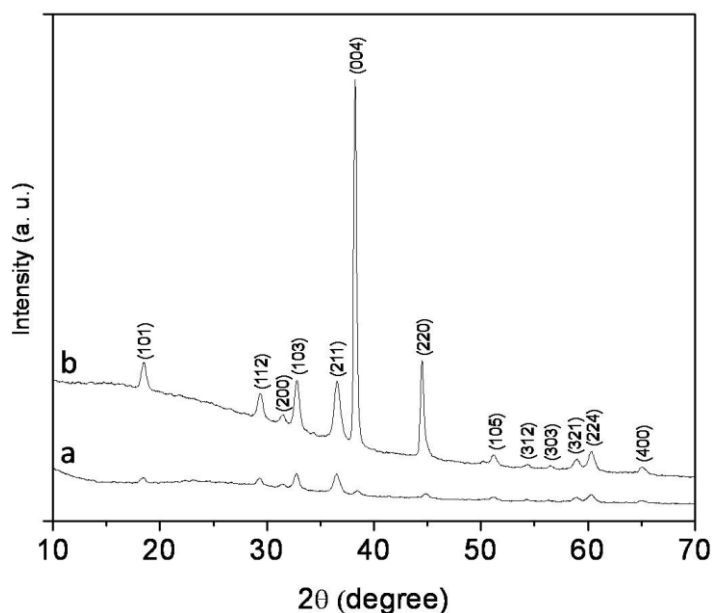

Fig. 3.4. X-ray diffraction patterns of manganese oxide/dye-surfactant hybrid assemblies (a) as-prepared and (b) after calcinations at 500 ^{0}C for 1 h in argon atmosphere.

The Mn$_3$O$_4$ structures are, further, characterised by their chemical transformation under thermal toughening condition (trace b). After heating at 500 ^{0}C in argon atmosphere for 1 h, the peaks become sharpened and in addition, no additional diffraction peaks are seen suggesting excellent crystalline quality of the manganese oxide particles.[56]

3.1.3.5. Thermogravimetric Analysis

Thermogravimetric analysis (Fig. 3.5) of the as-dried powder sample shows two weight loss steps in the curve: 3.5 wt% loss corresponding to the water desorption (up to 200 °C), and a weight loss of 17.5 wt
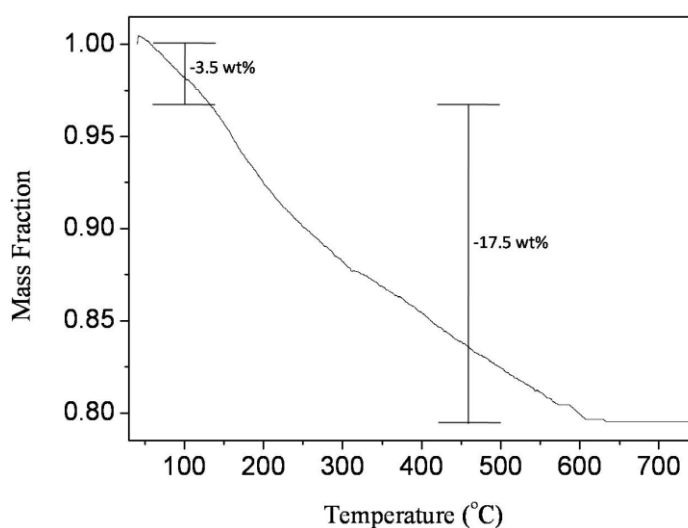

Fig. 3.5. Thermogravimetric analysis of the Mn$_3$O$_4$ microdandelions/dye-surfactant hybrid assemblies as-dried in air.

% over 200-800 ℃ as a result of the decomposition of dye/surfactant assemblies, verifying that the dye/surfactant conjugates are, indeed, incorporated into the microstructures.[57]Since amphiphilicity is the molecular basis of the self-assembly for thedye–surfactant systems, it is imperative that by tuning the amphiphilicity of the building blocks, the process of self-assembly could be manipulated.To interpret the relative importance of the amphiphilicity of the dye molecules in designing dye–surfactant assembly, the interaction of FITC–Dextran 2000S with the surfactant molecules has been elucidated. An unpredictably lower concentration of the CTAB solution is required to occur an indispensable interaction between the dye and surfactant molecules. As the formation of dye–surfactant aggregate is successful when the surfactant concentration is insufficient to form micelles and the sugar molecules are not surface-active, authenticates the importance of amphiphilicity of the dye molecules in manufacturing hybrid assembly to act as soft-template for preparation of manganese oxide superstructures.[49] A plausible mechanism of the formation of Mn_3O_4 microdandelions using dye-surfactant composites could be enunciated as follows. Addition of manganese acetate precursor to the dye-surfactant mixture results in the binding of Mn(II) to the dye-surfactant conjugates[58]and subsequent hydrolysis governs the formation of Mn_3O_4 microstructures with dandelions-like morphology.[59]

3.1.3.6. Schematic Presentation Showing the Formation of the Microdandelions at the Dye-Surfactant Assemblies

A schematic presentation of the evolution of Mn_3O_4 microdandelions using dye-surfactant composites is shown in Scheme 3.1.
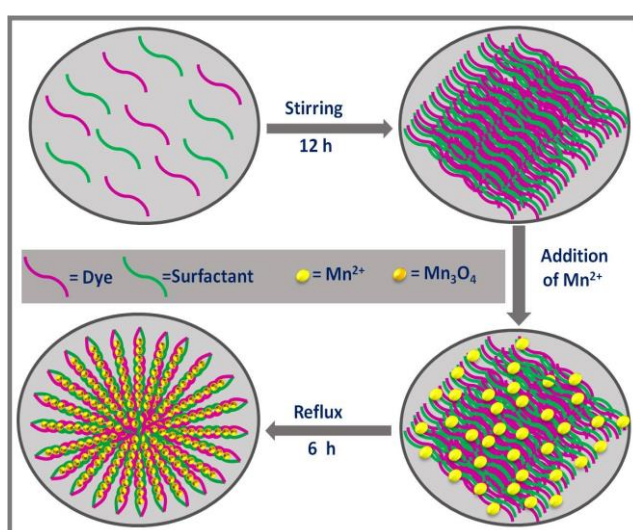
Scheme 3.1.Schematic presentation showing the formation of Mn_3O_4 microdandelions at the dye-surfactant assemblies.

3.1.3.7. Study of the Textural Properties by BET Surface Area Measurements

The textural properties of the as-dried powder sample of Mn_3O_4 microdandelions have been characterised by Brunauer–Emmett–Teller (BET)[60] gas-sorption measurements performed at 77 °K under vacuum. The specific surface area and Langmuir surface area of the microstructures have been measured to be *ca.* 15.76 and 25.81 m² g⁻¹, respectively which are higher than that of the commercial Mn_3O_4 (0.9±1.8 m² g⁻¹).[61] Therefore, it is evident that Mn_3O_4 microdandelions, synthesised in the present experiment, manifest higher BET surface area to provide a platform for the photocatalytic degradation of organic dye molecules.[62] A comparative account of the surface area in the bulk and nano dimension of the Mn_3O_4 microdandelions and some other manganese oxides-based catalysts[53,61,63] is shown in Table 3.1.

Table 3.1. A comparative account of the surface area in the bulk and nano dimension of the Mn_3O_4 microdandelions and some other manganese oxides based catalysts
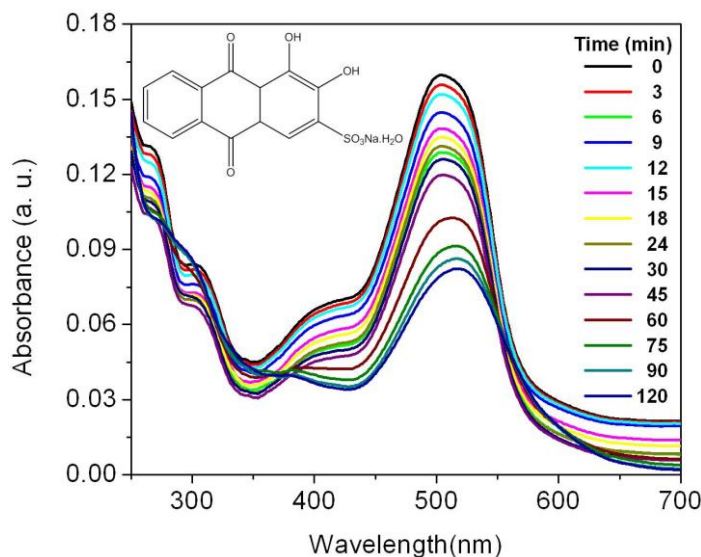
Materials size the bulk	Particle size nano dimension (nm)	Surface area in the bulk (m²g⁻¹)	Surface area in nano dimension (m²g⁻¹)	Nano-to-bulk ratio	Particles employed in physicochemical processes	Reference
Mn_3O_4 nanoparicles	23 ± 2.7	0.9 ± 1.8	40.9 ± 0.9	45.44	–	Sahu et al. [61]
Mn_2O_3 nanorods	1000 ± 300, 50 ± 10	1.1 ±2 .0	22.27	20.24	Selective oxidation of alcohols to aldehydes	Rahaman et al. [53]
α -MnO_2 nanorods	1000 ± 300, 50 ± 10	1.4 ± 1.0	14.15 ± 1.8	10.10	Cathode materials for sodium ion batteries	Su et al. [63]
β -MnO_2 nanorods	1000 ± 300, 50 ± 10	1.9 ± 1.0	33.54 ± 0.5	17.65	Cathode materials for sodium ion batteries	Su et al. [63]
Mn_3O_4 microdandelions	1000 ± 200	0.9 ± 1.8	25.8 ± 1.0	28.67	Photodegradation of alizarin red	Present work

3.1.3.8. Photocatalytic Degradation of Alizarin Red under Visible Light

To assess the photocatalytic activity of these Mn_3O_4 microstructures, the degradation of alizarin red was selected as the model reaction. Alizarin red or 1,2-dihydroxyanthraquinone, also known as 'Turkey Red', is an organic dye belonging to alizarin family, derived from the roots of plants of the madder genus and has been used as a prominent red dye, especially, for dyeing textile fabrics.[64] The photocatalytic degradation of alizarin red was employed as the model reaction as its degradation can, easily and quantitatively, be monitored via its absorption spectroscopy. Moreover, alizarin red was chosen because of its high stability against spontaneous photobleaching in the absence of a photocatalyst.[65] In the photocatalytic reaction, 25 μg of the as-prepared catalysts was dispersed with 3.0 mL of 2.0 μM aqueous solution of the dye molecules and the progress of the reaction was followed in the absorption spectrophotometer. Fig. 3.6 shows the absorption spectral changes during the

photocatalytic degradation of alizarin red in aqueous medium. The molecular structure of the dye is shown in the inset. The dye molecules exhibit a very intense absorbance band centered around 503 nm along with a less intense vibrational shoulder, centered around 308 nm corresponding to n $\rightarrow \pi^*$ and $\pi \rightarrow \pi^*$ transitions and molar extinction coefficient, $\varepsilon \sim 29,100$ M^{-1} cm^{-1} corresponding to the monomeric form of the dye.[66] As controls, an aqueous solution of alizarin red (3.0 ml, 2.0 μM) was exposed to the same tungsten lamp under identical experimental conditions. It was observed that, in the absence of the catalysts, the degradation of the dye is very slow in the experimental time

Fig. 3.6. Absorption spectral changes of aqueous solution of alizarin red (2.0 μM) in the presence of 25 μg Mn$_3$O$_4$ under visible light irradiation. Inset shows the molecular structure of the dye.

scale. To check whether absorbance decrease is a result of alizarin red absorption, we have mixed the dye and Mn$_3$O$_4$ microdandelions at the experimental concentrations and allowed to equilibrate overnight under vacuum. Only a slight decrease in the absorbance of the dye was seen; thus, the possibility of the absorbance decrease as a result of alizarin red absorption could be ruled out. As control experiment, the influence of only FITC-D 2000S or CTAB at the concentrations that may be present in the microdandelions employed for the photocatalytic reaction has been tested. It was noted that pure dye or surfactant does not bear any influence on the photocatalytic degradation of the dye molecules.

The degradation of the dye, also, does not take place in the absence of light. Therefore, it could be conceived that Mn$_3$O$_4$ microstructures are indispensable for the visible light-assisted degradation of the dye molecules. In the presence of Mn$_3$O$_4$ microdandelions, alizarin red molecules start to degrade upon visible light illumination. With increase in irradiation time, the intensity of alizarin red ($\lambda_{max} \sim 505$ nm) decreases sharply. After a certain time (t = 30 min), the intensity at 505 nm decreases and the intensity at 270 and 295 nm increases. These changes in the

absorption spectral features indicate that with increase in irradiation time alizarin red undergoes photocatalytic degradation and formssmall fragmented organic products.[31,36]

Under visible light irradiation, dyes rather than Mn_3O_4 particles are excited by visible light to appropriate singlet and triplet states, subsequently, followed by electron injection from the excited dye onto the conduction band of metal oxides, whereas the dyes are converted to the cationic dye radicals, dye[.+].[31] The injected electron of Mn_3O_4 (e^-) reacts with pre-adsorbed O_2 to form

Fig. 3.7. Plot of $\ln(A_0/A)$ as a function of time for the degradation of alizarin red in the absence and presence of Mn_3O_4 microdandelions under visible light irradiation.

oxidising species ($O_2^{.-}$, $HOO^.$ and then $^.OH$ radicals) that can bring about photooxidations. The major component of the peroxides produced is H_2O_2, CO_2 and to smaller carbonyl species; the principal intermediate produced is phthalic acid.[31] Thus, metal oxide nanoparticles play an important role in electron transfer mediation, even, though itself is not excited. Profile showing the plot $\ln(A_0/A)$ where, A_0 is the

absorbance at $t = 0$ and A the absorbance at time $t = t$, as a function of time is presented in Fig. 3.7. It is, apparent, that the reaction follows first-order kinetics and corresponding rate constants were calculated to be 1.9×10^{-4} and 6.7×10^{-3} min^{-1} in the absence and presence of the catalysts, respectively which indicate that the rate of reaction

Fig. 3.8. Histogram showing the percentage of the degradation of the dye in each cycle.

is enhanced by approximately 35 times in the presence of the Mn_3O_4 microdandelions. In this reaction, Mn_3O_4 microdandelions act as heterogeneous catalysts which are inorganic materials.[67,68] It is observed that the catalysts could be reused up to six cycles
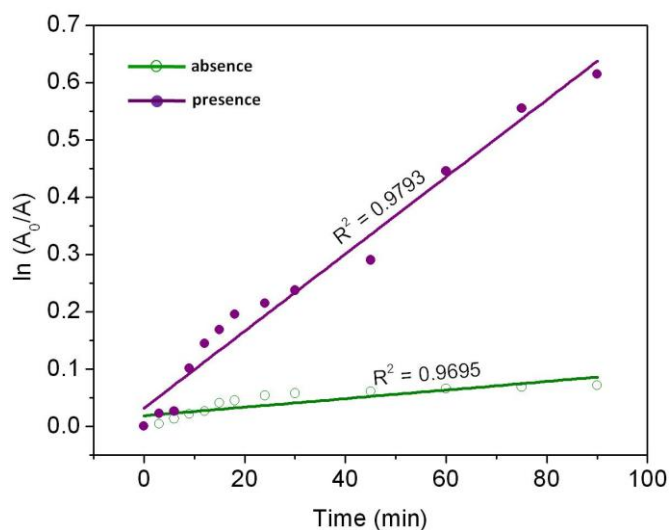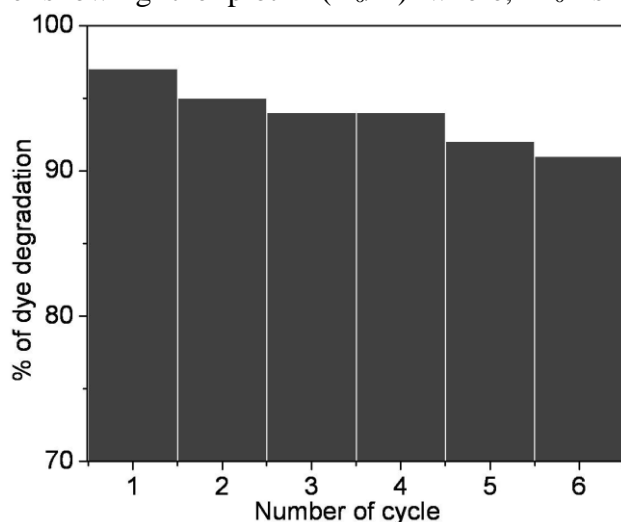
of operations without any apparent loss of activity. Therefore, the catalysts were separated from the reaction mixture by centrifugation or natural sedimentation at the end of the degradation reaction and subsequent drying in air. A histogram showing the percentage of the degradation of the dye in each cycle is presented in Fig.3.8.

A comparative account of the nano/microstructured catalysts for thephotocatalytic degradation of alizarin red under visible light irradiation has been presented in Table3.2. Therefore, it could beconceived that Mn_3O_4 microdandelions could be employed as alternative catalysts for the degradation of alizarin red under visible light irradiation.

Table 3.2. A comparative account of the catalytic activity of the visible light photocatalysts for alizarin red degradation

Catalysts	Particle size (nm)	Reaction conditions	Catalyst loading (g L^{-1})	Reaction rate (min^{-1})	Reference
TiO$_2$ nanostructures	8 ± 2	500 W halogen lamp	0.5	0.084	Liu et al.[30]
Bi-doped TiO$_2$	30 ± 10	150 W Philips bulb, wavelength 420-520 nm	0.025	0.0232	Soodet al.[31]
CdS nanostructures	–	pH~8.4	0.05	0.0169	Patilet al.[34]
TiO$_2$-In$_2$O$_3$ nanocomposites		8–12 Pen Ray lamp of 4,400 μW cm^{-2}	0.1	0.0058	Rodríguez-González et al.[35]
TiO$_2$	10–12	Photolysis, ultrasonication	0.03	0.0225	Vinuet al.[39]
Mn$_3$O$_4$ microdandelions	1000 ± 200	60 W tungsten bulb, room temp.	0.008	0.0067	Present work

3.1.4. Conclusion

In conclusion, the cumulative effect of the FITC-dextran 2000S/CTAB assemblies have been exploited for synthesis of high surface area Mn_3O_4 microdendelions. The microstructures were found to act as effective catalysts for the degradation of alizarin red under visible light illumination. The dye-surfactant conjugates could be exploited as soft-templated system for the synthesis of other inorganic materials with controlled morphological superstructures and unusual functionalities.

3.2. Soft-Templated Synthesis of Mn₂O₃ Nanorods for Selective Transformation of Alcohols to Aldehydes

3.2.1. Introduction

Catalyst is the work-horse in synthetic chemistry.[69-71] The robust reactivity and selectivity of catalyst lead to efficient transformation of raw materials into the desired pharmaceuticals, fuels, agrochemicals, pigments, polymers, commercial and natural compounds, which are essential for our highly demanding modern society. In this context, nanomaterials have tremendous potential to serve as significantly improved catalysis performance because of their active surface and interfacial atom effect, innovative new chemical property, high reactivity, low catalyst loading, environmentally benign nature, easy recovery and reusability.[72-76] In recent years, size and shape-controlled synthesis of manganese oxides (MnO_x) nanomaterials has fascinated considerable interest from both academia and industry due to tuneable physicochemical properties,[77-80] high-density magnetic storage media,[81] ion-exchange,[82] molecular adsorption,[83] electronics,[84] biosensors,[85] energy storage,[86] batteries[87] and catalysts.[88] Manganese oxides are the most attractive inorganic materials owing to their structural flexibility and availability of different oxidation states of manganese (II, III, IV) that have envisaged their structural, transport and magnetic properties[89-92] in a diverse range of niche applications.[93-95] Among the different oxidation states of manganese oxides, Mn_2O_3 is well known as cheap and environment-friendly catalyst and could be employed as ideal candidate for the removal of CO and NO_x from waste gas,[96] decomposition of H_2O_2 into hydroxyl radicals in the catalytic peroxidation of organic effluents[97] and as an oxygen storage component.[98] Although, catalytic activities over transition metal oxide catalysts are lower than those over noble metal catalysts, the inherent advantages of metal oxide catalysts, such as, low cost, high thermal stability, and high mechanical strength, which make them a promising alternative for outstanding catalytic applications.[99] While the catalytic activity of these materials at the nanoscale dimension depends strongly on their surface properties, the reactivity and selectivity of nanoparticles can be tuned through controlling the morphology because the exposed surfaces of the particles have distinct crystallographic planes depending on

their shape.[100] Therefore, synthesis of Mn_2O_3 nanoparticles with well-controlled morphology and a narrow size distribution is desirable for achieving practical applications, such as, catalysis.

Diverse synthetic approaches have been implemented in the literature for the fabrication of size and shape-selective Mn_2O_3 nanostructures and exploited their physical and chemical properties in a wide range of applications. Ganguli and co-authors prepared nanorods of anhydrous manganese oxalate as precursor to synthesize single phase nanoparticles of various manganese oxides, such as, MnO, Mn_2O_3 and Mn_3O_4 under specific reaction conditions and studied their field-dependent magnetization properties.[101] Han and co-workers have reported the synthesis of Mn_2O_3 nanocrystals by the thermolysis of manganese(III) acetyl acetonate on a mesoporous silica, SBA-15 and the nanocomposites showed significant catalytic activity toward CO oxidation below 523 K.[102] Chen and He have described facile synthesis of mono-dispersed Mn_2O_3 nanostructures by treating a mixture of $KMnO_4$ solution and oleic acid at low temperatures (below 200 °C) and shown the application of these particles as efficient water purifier.[103] Polshettiwar and colleagues have devised a simple strategy using aqueous solution of $K_3[Mn(CN)_6]$ under microwave irradiation to afford the nanomaterial.[80] Gnanam and Rajendran have described the preparation of α–Mn_2O_3 nanoparticles by dropwise addition of an aqueous ammonia solution to manganese(II) chloride tetrahydrate ($MnCl_2.4H_2O$) in methanol under vigorous stirring and reported the optical properties of the synthesized materials.[104] Yang and colleagues reported the size-controlled synthesis of monodispersed Mn_2O_3 octahedra assembled from nanoparticles by a mediated *N,N*-dimethylformamide solvothermal route and the particles were found to exhibit catalytic activity towards CO oxidation.[105] Qiu et al. have described the synthesis of hierarchically structured Mn_2O_3 nanomaterials with different morphologies and pore structures from precursor containing the target materials interlaced with the polyol-based organic molecules and examined their potential as anode materials for lithium ion batteries.[106] Cao et al. have reported large-scale Mn_2O_3 homogeneous core/hollow-shell structures with cube-shaped and dumbbell-shaped morphologies and the particles were found to exhibit excellent performance in waste water treatment.[107] Najafpour and colleagues have described the synthesis of nano-sized Mn_2O_3 particles by decomposition of aqueous solution of manganese nitrate at 100 °C and it was observed that the particles possessing catalytic activity towards water oxidation and epoxidation of olefins in the

presence of cerium(IV) ammonium nitrate and hydrogen peroxide, respectively.[108] We envisioned fabrication of Mn_2O_3 nanorods by the soft-templated strategy which will provide roughened high surface area to offer an ideal platform for high and innovative chemical activity towards novel catalysis processes such as most demanding direct synthesis of aldehydes and ketones from alcohols under oxidative conditions.

3.2.2. Experimental

3.2.2.1. Synthesis of Manganese Oxide Nanorods in Polymer-Surfactant Conjugates

The nanostructures of manganese oxide have been synthesised using polymer-surfactant conjugates and manganese acetate tetrahydrate as the precursor salt. In a typical synthesis, an aliquot of aqueous polyethylene glycol (PEG) (0.4 mM) was added to an aqueous solution of sodium dodecyl sulphate (SDS) (2.0 mM) in a double-necked round-bottom flask so that the total volume of the solution is 25 mL and the mixture was stirred overnight at room temperature. Now, an amount of 0.245 g $Mn(ac)_2.4H_2O$ was dissolved in the polymer-surfactant mixture by refluxing on a water bath at 65°C. After complete dissolution of the precursor, 100 μL diethanolamine was added and refluxing was continued for another 6 h. After about 30 min, the reaction mixture, suddenly, turned into yellowish brown from a colourless solution indicating the formation of manganese oxide nanostructures. As the refluxing was continued, the colour slowly changed into deep brown pointing out to the aggregation between the ultrasmall manganese oxide particles to rod shaped nanostructures. The water-bath was removed and the reaction mixture was stirred for 12 h at room temperature. The particles formed by this method was washed five times with slightly hot water and finally, dispersed in water. The manganese oxide nanostructures prepared by this method are stable for a month and can be stored in the vacuum desiccator without any significant agglomeration or precipitation of the particles.

3.2.2.2. General Procedure for Synthesis of Aldehydes

The precursor alcohol (1 mmol), Mn_2O_3 (1.6 mg, 0.01 mmol), $PhI(OAc)_2$ (403 mg, 1.25 mmol) and $MgSO_4$ (about 300 mg) were taken together in ethylenedichloride (EDC, 25 mL) and stirred magnetically at 45 °C until the reaction was complete. The progress of the reaction was monitored by TLC. After completion of the reaction the

post reaction mixture was filtered through a sintered funnel and the residue was washed with EDC (2×5 mL). The combined EDC was transferred to a separating funnel, washed with water (3×10 mL) and dried using activated $MgSO_4$. The solvent was removed in a rotary evaporator at room temperature under reduced pressure. The crude product was purified by column chromatography over silica gel (60–120 mesh) using ethyl acetate-petroleum ether as eluent to afford the desired aldehyde and corresponding acid byproduct. Thus, the reaction of benzyl alcohol (1a, 109 mg, 1.0 mmol) afforded benzaldehyde (2a) and benzoic acid (3a) after purification by column chromatography on silica gel (60-120 mesh) with ethyl acetate-petroleum ether (1:200, v/v) as an eluent in an yield of 87% (92.5 mg, 0.87 mmol) and 4% (4.5 mg, 0.04) respectively. The structure of the desired product (2a) and byproduct (3a) were confirmed with the help of the available literature boiling and melting points and also comparing the recorded NMR (^{1}H and ^{13}C), FT-IR, and mass (HR-MS) spectra. Similarly other aldehydes (2b-e), ketones (4a,b), acids (3a-f) and sugar aldehyde (2f) were characterized by measuring melting/boiling points, recording NMR (^{1}H and ^{13}C), FT-IR, and mass (HR-MS) spectra and optical rotation, which were verified with the know literature data and spectra.

3.2.3. Results and Discussion

From the literature survey, here in this portion, we have reported an innovative fabrication approach to rod-shaped Mn_2O_3 microstructures using polymer/surfactant assembly as soft-template and their characterisation by absorption spectroscopy, Fourier transform infrared spectroscopy, transmission electron microscopy, high resolution transmission electron microscopy, scanning electron microscopy, energy dispersive X-ray analysis, selected area electron diffraction, X-ray diffraction analysis, Raman, Brunauer–Emmett–Teller surface area measurements and thermogravimetric techniques. An innovative catalytic property of the Mn_2O_3-microrods is discovered towards selective oxidation of alcohols to valuable aldehydes, chiral analogue and ketones using phenyliodoacetate [PhI(OAc)$_2$] as an oxidizing agent.

3.2.3.1. Absorption Spectroscopy

The absorption spectral features of the as-synthesized Mn_2O_3 sample in the solid state are shown in Fig.3.9. The estimated direct band gap of the Mn_2O_3 was found to be 1.29 eV; this value is almost close to reported value of the Mn_2O_3
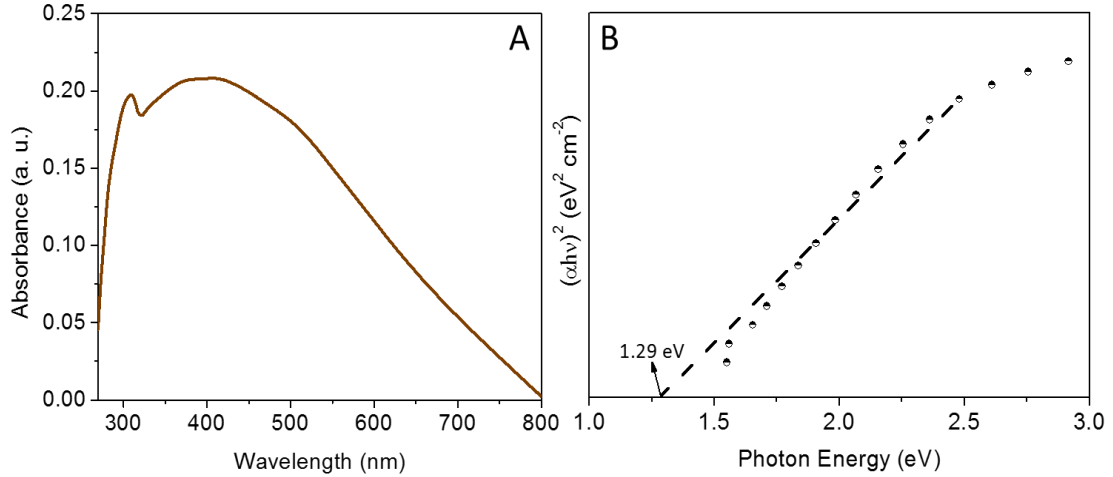

Fig. 3.9. Solid state absorption spectrum of manganese oxide superstructures in polymer-surfactant conjugates.

nanostructures.[116] A clear band edge at 325 nm is characteristic of Mn-O vibration. The direct band gap energy (E_g) for the manganese oxide superstructures could be determined by fitting the absorption data to the direct band gap transition equation as,[117]

$$(\alpha h\nu)^2 = A(h\nu - E_g) \tag{3.1}$$

where, α is the absorption co-efficient, $h\nu$ the photon energy and A a constant. The absorption coefficient (α) is defined as: $\alpha = 2.303 \, A/L \, c$, where, A is the absorbance of the sample, c the loading of sample (g L^{-1}), L the path length (= 1 cm). Profile showing a plot of $(\alpha h\nu)^2$ as a function of $h\nu$ is shown in panel b and the extrapolation of linear portions of the curve towards absorption equal to zero offers a measure of the direct band gap transitions, E_g. The estimated direct band gap of the Mn_2O_3 was found to be 1.29 eV; this value is almost close to reported value of the Mn_2O_3 nanostructures.[118]

3.2.3.2. Morphology, Composition and Crystallinity of the Mn_2O_3 Nanorods

The morphology, composition and crystallinity of the particles synthesized in the polymer/surfactant mixture are presented in Fig. 3.10. Representative scanning electron micrograph (trace a) of the Mn_2O_3 particles shows bunch of elongated
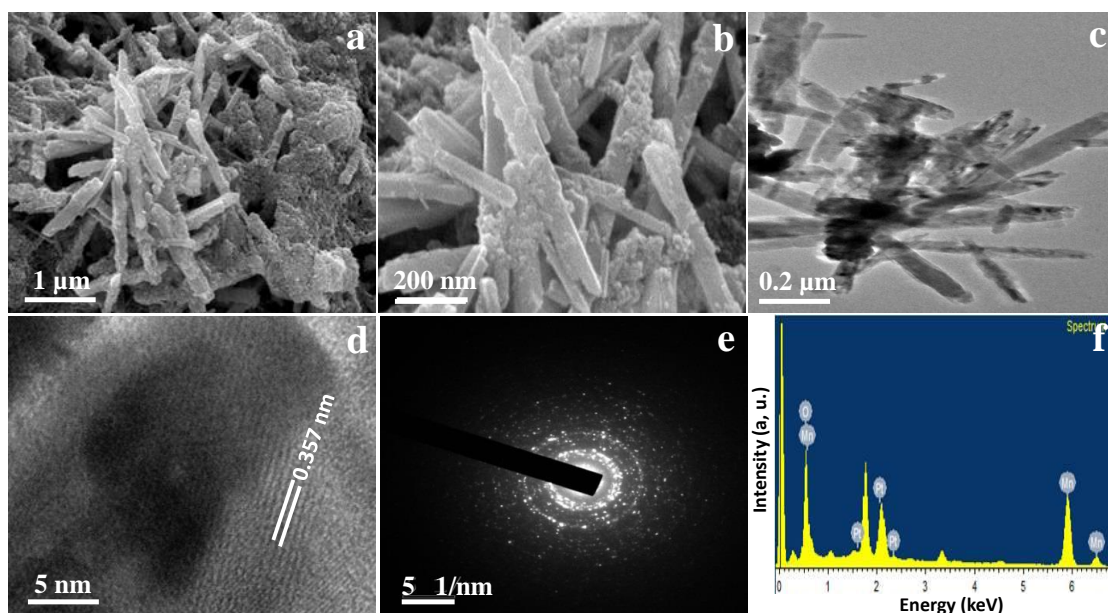

Fig. 3.10. (a) Scanning electron micrograph, (b) high resolution scanning electron micrograph, (c) transmission electron micrograph, (d) high resolution transmission electron micrograph, (e) selected area electron diffraction pattern, and (e) energy dispersive X-ray analysis of the manganese oxide microrods in polymer-surfactant conjugates.

nanorods with length up to 1 ± 0.3 μm and width 50 ± 10 nm. To further examine the surface morphology of the microstructures, high magnification SEM images were recorded (trace b) and it was apparent that the surface of the particles was with roughened edge, which indicates the growth and slow transformation to rod-shaped nanostructures occur through oriented aggregation of primary nanocrystals. At the very beginning of reflux, the concentration of reactants is comparatively high; therefore, some nuclei can be formed very fast resulting in the occurrence of ultrasmall particles. The nuclei, subsequently, orient and grow fast along the (211) direction to form one dimensional nanorods.[117] The size and shape of the nanocrystals is further evident from the transmission electron micrographs (panel c) of the Mn_2O_3 particles formed in the polymer/surfactant assembly. High resolution TEM image (panel d) of the Mn_2O_3 nanorods displays the interplanar distance between the fringes about 0.357 nm which corresponds to the distance between the (211) planes of the Mn_2O_3 crystal lattice.[50] Selected area electron diffraction pattern (panel e) of the Mn_2O_3 nanostructures is consistent with strong ring patterns due to (211), (222) and

(400) planes and therefore, confirms the crystallinity of the materials.[118] Representative energy dispersive X-ray spectrum (panel f) of Mn_2O_3 nanorods indicates that the particles are composed of Mn and O elements.

3.2.3.3. Fourier Transform Infrared Spectroscopy

The formation of manganese oxide particles in the polymer-surfactant conjugates has been studied through FTIR spectroscopy (Fig.3.11). It is seen that the Mn–O bond stretching frequency appears in the range of 450–680 cm^{-1} along with two strong peaks at 630 and 525 cm^{-1} that arise due to the stretching vibration of Mn–O and Mn–O–Mn bonds,[103] indicating the formation of Mn_2O_3 in the polymer/surfactant conjugates.[120]
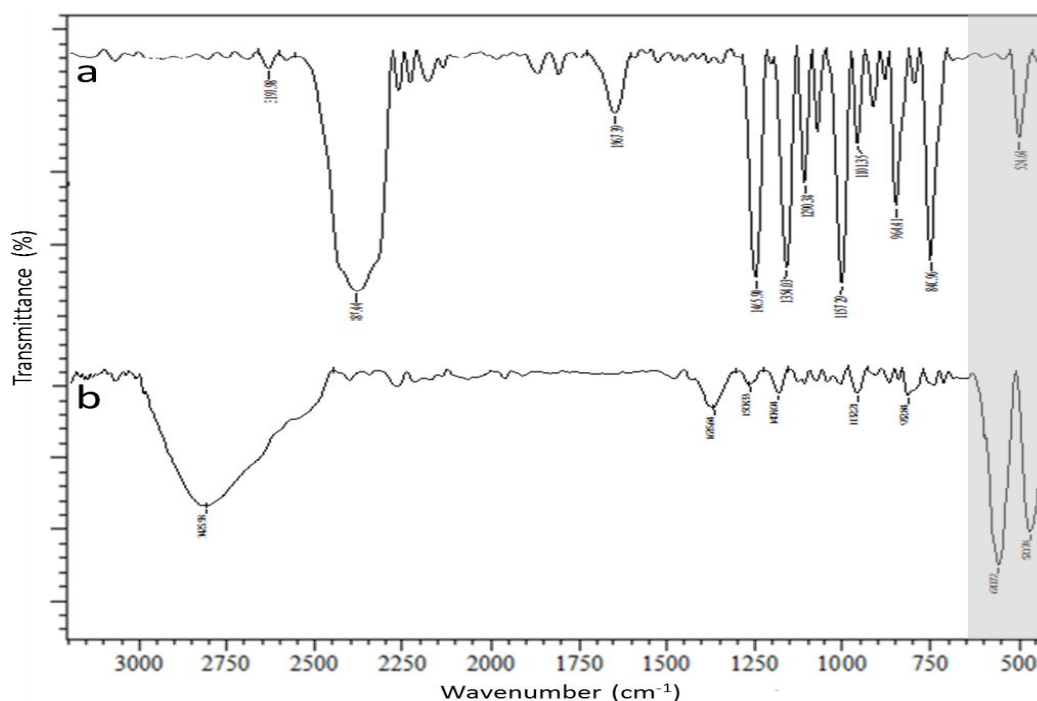
Fig. 3.11. FTIR spectra of (a) polyethylene glycol/sodium dodecyl sulphate conjugates and (b) after formation of Mn_2O_3 nanostructures in PEG/SDS soft templates at room

3.2.3.4. X-ray Diffraction Pattern

The X-ray diffraction pattern of the of the representative hybrid rod-shaped assemblies is shown in Fig.3.12; all diffraction peaks implying a crystalline structure are consistent with the standard values of bulk Mn_2O_3[JCPDS No-41-1442].[102] The

Mn_2O_3 structures are further characterized by their chemical transformation under thermal toughening condition. The intensity of Mn_2O_3 peaks are weak or masked due to presence of organics on the surface of the Mn_2O_3 nanorods. After heating at 800 ^{0}C in argon atmosphere for 6 h, the peaks become sharpened indicating bixbyite phase of Mn_2O_3 and in addition, no additional diffraction peaks

Fig.3.12.X-ray diffraction pattern of (a) manganese oxide/polymer-surfactant hybrid assemblies and (b) after calcination of the assemblies at 800 ^{0}C in argon atmosphere for 6 h.

appeared suggesting excellent crystalline quality of the Mn_2O_3 particles.[102]

3.2.3.5. Raman Spectrum

Fig. 3.13 shows the Raman spectrum of the as-prepared nanorods under ambient condition. The structure of Mn_2O_3 belongs to Ia_3 symmetry group with $a = 9.41$ and possess cubic bixbyite structures.[121] The bands at 310, 366 and 655 cm^{-1} could be ascribed to the out of-plane bending modes of Mn_2O_3, the asymmetric stretch of bridge oxygen species (Mn–O–Mn) and the symmetric stretch of Mn_2O_3 respectively[122, 123] in

Fig. 3.13. Raman spectrumof the manganese oxide/polymer-surfactant hybrid assemblies dried in air.

correspondence to that obtained for bulk MnO_x particles.[124]

48

3.2.3.6. Thermogravimetric Analysis

Fig. 3.14 shows thermogravimetric analysis of the as-dried powder sample shows two

weight loss steps in the curve: 8.9 wt% loss corresponding to the water desorption (up to 200 °C), and a weight loss of 32.1 wt % over 200-800 ºC as a result of the decomposition of polymer/surfactant assemblies, verifying that the polymer/surfactant conjugates are, indeed, incorporated into the nanostructures.[57].
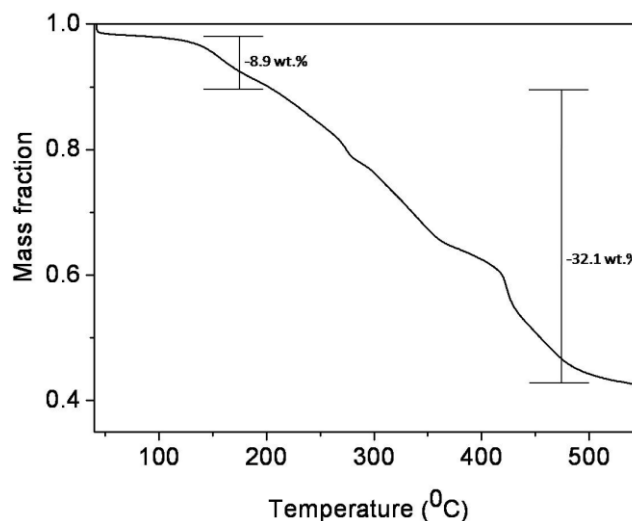

Fig. 3.14. Thermogravimetric analysis of the manganese oxide/polymer-surfactant hybrid assemblies as-dried in air.

3.2.3.7. Surface Area Measurement by Brunauer–Emmett–Teller (BET) Method

The textural properties of the Mn_2O_3 microrods were investigated by Brunauer–Emmett–Teller (BET) gas-sorption measurements performed at 77 °K of the as-dried

powder sample under vacuum as shown in Fig.3.15. The specific surface area and Langmuir surface area of the microrods have been measured to be *ca.* 13.60 m^2 g^{-1} and 22.27 m^2 g^{-1}, respectively from which it is evident that Mn_2O_3 nanorods, synthesised in the present experiment,
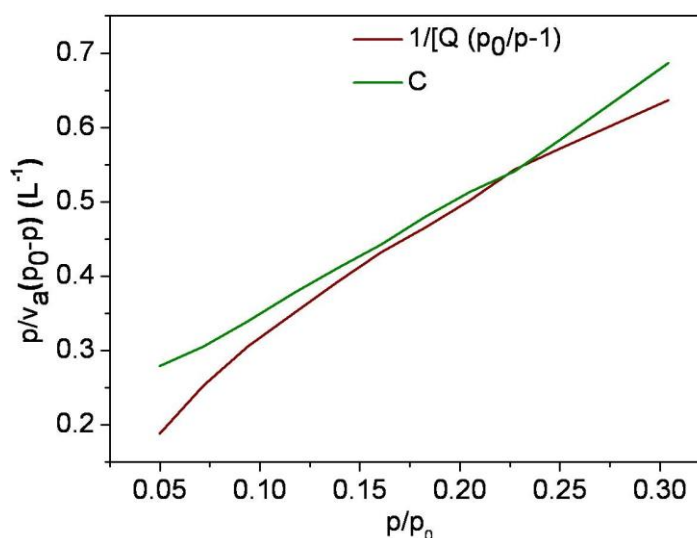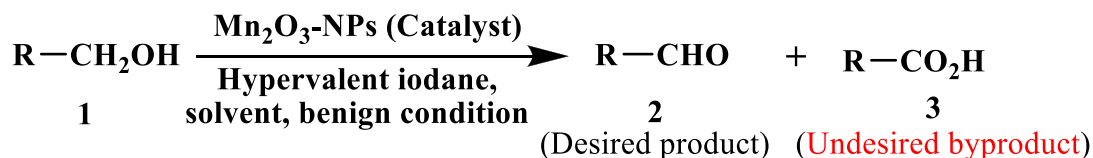

Fig. 3.15. BET adsoption isotherm for N_2 gas-soprtion of the manganese oxide/polymer-surfactant hybrid assemblies dried in air.

manifest high BET surface areas to provide a platform for the catalytic organic transformation.[98,126]

$$\frac{p}{p(p_0 - p)} = \frac{1}{v_m c} + \frac{c-1}{v_m c}\frac{p}{p_0} \quad (3.2)$$

where, v is the volume of the gas adsorbed under pressure p, when p_0 is the saturated vapour pressure at the same temperature, v_m the volume of the gas adsorbed to form a unimolecular layer and c a constant for a given adsorbate. From a plot *of p/v(p₀-p) vs. (p/p₀)*, the specific surface area and Langmuir surface area of the microrods have been measured to be *ca.* 13.60 m^2 g^{-1} and 22.27 m^2 g^{-1}, respectively which are higher than that of the commercial Mn$_2$O$_3$ (3.9 m^2 g^{-1}) Therefore, it is evident that Mn$_2$O$_3$ nanorods, synthesized in the present experiment, manifest high BET surface areas to provide a platform for the catalytic organic transformation.

3.2.3.8. Catalytic Direct Synthesis of Aldehydes using Mn$_2$O$_3$ Rods

In the initial experiments, we have decided not to apply high temperature for the desired catalytic oxidation (Scheme 3.2) of our model substrate benzylalcohol (**1a**, R= Ph, Table 3.3) to benzaldehyde (**2a**) using λ^3-hypervalent iodane,[114,115,128] so that the possibility of forming byproduct benzoic acid (**3a**, entry 1, Table 2) could be avoided.

$$R-CH_2OH \xrightarrow[\substack{\text{Hypervalent iodane,}\\ \text{solvent, benign condition}}]{\text{Mn}_2\text{O}_3\text{-NPs (Catalyst)}} R-CHO \quad + \quad R-CO_2H$$

<div align="center">

1   **2**   **3**

(Desired product)   (Undesired byproduct)

</div>

Scheme 3.2. Direct synthesis of aldehydes using Mn$_2$O$_3$-microoorods catalyst

After several experiments using as-synthesised Mn$_2$O$_3$ nanorods (1 mol%) we discovered its catalytic property for the oxidative dehydrogenation reaction using PhIO[46] (1.25 mmol), which revealed about 60% conversion at 50 °C to afford benzaldehyde (**2a**; yield: 45%) with high selectivity (**2a**:**3a** = 9:1). The yield (68%) was improved on use of PhICl$_2$ (entry 2). Gratifyingly utilizing commercially available PhI(OAc)$_2$[115] the conversion (100%), reaction rate (2 h), yield (96%) and selectivity (**2a**:**3a** = 47:3) were significantly improved under the similar reaction conditions (entry 3). The optimized oxidation process was found utilizing as low as 0.01 mol% of the nanorods as described in the entry 7, which was obtained (entries 5-8) by changing the reaction temperature (50-40 °C) and catalyst loading (1-0.005). The reaction rate (70% in 12 h), yield (48%) and selectivity (**2a**:**3a** = 2:3) were drastically reduced in absence of the Mn$_2$O$_3$-NPs (entry 9). Ethylene dichloride was found as the suitable solvent because the other polar aprotic solvents such as

dichloromethane (CH$_2$Cl$_2$), tetrahydrofuran (THF) and acetonitrile (entries 10-12), nonpolar toluene (entry 13) and protic methanol or water (entries 14,15) were not effective for the unprecedented catalytic process. The diverse catalytic activity of the Mn$_2$O$_3$-nanorods was evaluated utilizing various types of alcohols under the optimized reaction conditions (entry 1, Table 2). The benzyl alcohols bearing activated (**1b**) and deactivated (**1c**) aromatic moiety (entries 2,3, Table 2) were tolerated in this reaction to afford corresponding aldehyde with excellent yield and selectivity (entries 2,3). Interestingly in presence strongly electron withdrawing -NO$_2$ group the reaction rate was enhanced (from 4.5 to 3 h) with respect to activated aromatic nucleus (**1b**), which simultaneously reduced the selectivity from 19:1 to 23:2 (entries 2,3).

3.2.3.9. Optimization of Mn$_2$O$_3$-Nanorods Catalysed Oxidation of Benzyl Alcohol to Benzaldehyde

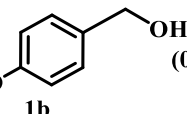**Table 3.3.** Development and Optimization of Mn$_2$O$_3$-Microrods Catalyzed Oxidation of Benzylalcohol to Benzaldehyde
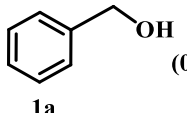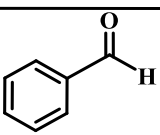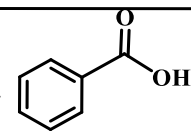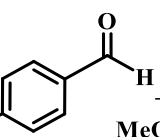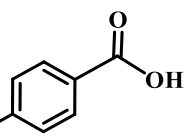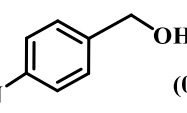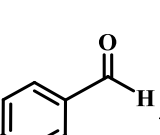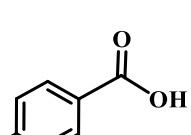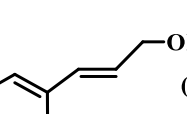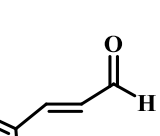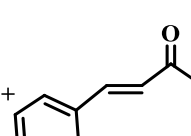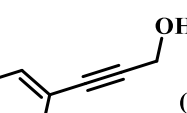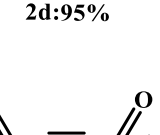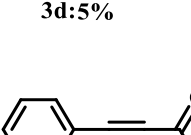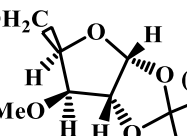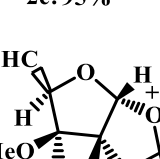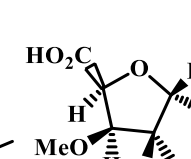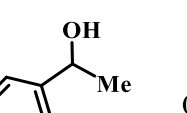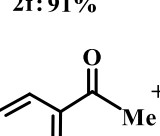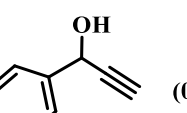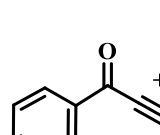
Entry	Catalyst (mol%)	Hypervalent iodane (1.25 eq.)	Reaction conditions	Reaction time	Conversion (%)	Yield(%); 2a:3a
1	1.0	PhIO	(CH$_2$Cl)$_2$, 50 °C, MgSO$_4$	12 h	60	45; 9:1
2	1.0	PhICl$_2$	(CH$_2$Cl)$_2$, 50 °C, MgSO$_4$	12 h	90	68; 23:2
3	1.0	PhI(OAc)$_2$	(CH$_2$Cl)$_2$, 50 °C, MgSO$_4$	2.0 h	100	93; 47:3
4	1.0	PhI(OAc)$_2$	(CH$_2$Cl)$_2$, 45 °C, MgSO$_4$	3.0 h	100	94; 24:1
5	1.0	PhI(OAc)$_2$	(CH$_2$Cl)$_2$, 40 °C, MgSO$_4$	24 h	95	81; 24:1
6	0.1	PhI(OAc)$_2$	(CH$_2$Cl)$_2$, 45 °C, MgSO$_4$	3.5 h	100	94; 24:1
7	**0.01**	**PhI(OAc)$_2$**	**(CH$_2$Cl)$_2$, 45 °C, MgSO$_4$**	**4.0 h**	**100**	**91; 24:1**
8	0.005	PhI(OAc)$_2$	(CH$_2$Cl)$_2$, 45 °C, MgSO$_4$	12 h	50%	38; 24:1
9	-	PhI(OAc)$_2$	(CH$_2$Cl)$_2$, 45 °C, MgSO$_4$	12 h	70	48; 2:3
10	0.01	PhI(OAc)$_2$	CH$_2$Cl$_2$, reflux, MgSO$_4$	12 h	90	78; 24:1
11	0.01	PhI(OAc)$_2$	THF, 45 °C, MgSO$_4$	5.0 h	100	88; 24:1
12	0.01	PhI(OAc)$_2$	CH$_3$CN, 45 °C, MgSO$_4$	5.0 h	100	85; 24:1

13	0.01	PhI(OAc)$_2$	PhCH$_3$, 45 °C, MgSO$_4$	12 h	50%	34; 23:2
14	0.01	PhI(OAc)$_2$	MeOH, 45 °C, MgSO$_4$	12 h	40%	30; 23:2
15	0.01	PhI(OAc)$_2$	H$_2$O, rt,	12 h	50	39; 24:1

3.2.3.10. Synthesis of Aldehydes, Sugar Aldehydes and Ketones using Mn$_2$O$_3$-Rods as Catalysts

The diverse catalytic activity of the Mn$_2$O$_3$-nanorods was evaluated utilizing various types of alcohols under the optimized reaction conditions (entry 1, Table 2). The benzyl alcohols bearing activated (**1b**) and deactivated (**1c**) aromatic moiety (entries 2,3, Table 3.4) were tolerated in this reaction to afford corresponding aldehyde with excellent yield and selectivity (entries 2,3). Interestingly in presence strongly electron withdrawing -NO$_2$ group the reaction rate was enhanced (from 4.5 to 3 h) with respect to activated aromatic nucleus (**1b**), which simultaneously reduced the selectivity from 19:1 to 23:2 (entries 2,3). Another interesting feature observed in this reaction is the high chemoselectivity. Even in presence of oxidation prone double and triple bond-bearing allyl (**1d**) and propargyl (**1e**) alcohols (entries 4,5) smoothly underwent oxidation to corresponding aldehydes with 90-92% yield and outstanding selectivity (19:1). We turned our attention applying the benign strategy for oxidation of sugar-based chiral alcohol (**1f**, entry 6) and under the similar reaction conditions it afforded corresponding optically pure aliphatic aldehyde (**2f**) with high yield (76%) and selectivity (91:9). The diverse catalytic activity of the Mn$_2$O$_3$-nanorods was also successfully exploited on functionalized secondary alcohols (**1g**, **1h**) to obtain corresponding ketons (**4a**, **4b**, entries 8,9) without formation of the byproduct benzoic acid (**3a**). The catalytic reaction was tested with bulk Mn$_2$O$_3$ and it was seen that the particles could not selectively transform the alcohols to aldehydes. A comparative account highlighting utility of Mn$_2$O$_3$ nanorods and some other catalysts[128-131] towards the oxidation of alcohols is presented in ESI 7. This unprecedented property of Mn$_2$O$_3$-nanorods under very low catalyst loading (0.01 mol%) provides new prospects and perspectives in catalysis towards discovery of new materials, innovative catalytic activity and novel organic transformation to afford functional molecules for our highly demanding modern society.

Table 3.4. Synthesized Aldehydes, Sugar Aldehyde and Ketones

Entry	Alcohol(1)	Catalyst	Reagent &conditions	Conversion (%)	Desired aldehyde(2) or ketone (4)	Acid(3)	Yield(%, 2:3)
1	1a	Mn₂O₃ (0.01 mol%)	PhI(OAc)₂, EDC, 45 °C 4.0 h	100	2a:96%	3a:4%	91 (24:1)
2	1b	Mn₂O₃ (0.01 mol%)	PhI(OAc)₂, EDC, 45 °C 4.5 h	100	2b:95%	3b:5%	89 (19:1)
3	1c	Mn₂O₃ (0.01 mol%)	PhI(OAc)₂, EDC, 45 °C 3.0 h	100	2c:92%	3c:8%	95 (23:2)
4	1d	Mn₂O₃ (0.01 mol%)	PhI(OAc)₂, EDC, 45 °C 4.0 h	100	2d:95%	3d:5%	90 (19:1)
5	1e	Mn₂O₃ (0.01 mol%)	PhI(OAc)₂, EDC, 45 °C 4.0 h	100	2e:95%	3e:5%	92 (19:1)
6	1f	Mn₂O₃ (0.01 mol%)	PhI(OAc)₂, EDC, 45 °C 4.0 h	100	2f:91%	3f:9%	76 (91:9)
7	1g	Mn₂O₃ (0.02 mol%)	PhI(OAc)₂, EDC, 45 °C 6.0 h	100	4a:92%	3a (Not detected)	
8	1h	Mn₂O₃ (0.02 mol%)	PhI(OAc)₂, EDC, 45 °C 5.0 h	100	4b:94%	3a (Not detected)	

53

3.2.4. Conclusion

In conclusion, hydrolysis of manganese precursor in the presence of polymer/surfactant soft template has been found to be an effective strategy for the fabrication of Mn_2O_3 nanorods. The nanorods are crystalline and offer roughen surface and large surface area that installs new and innovative catalytic activity such as direct synthesis of valuable aldehydes through oxidation of alcohols in a highly chemoselective fashion. This new synthetic strategy for low dimensional manganese oxide material could be exploited for fabrication of novel inorganic materials with controlled superstructures and unusual functionalities. This unprecedented catalytic activity of Mn_2O_3 nanorods provides new prospects and perspectives in catalysis for the pursuance of novel organic transformations to afford functional molecules for our highly demanding modern society.

3.3. References

1. N. A. Kotov, In *Nanoparticle Assemblies and Superstructures* 2005, CRC Press, Boca Raton, USA.

2. M. Grzelczak, J. Vermant, E. M. Furst and L. M. Liz-Marzán, *ACS Nano*, 2010, **4,** 3591–3605.

3. H. Cölfen and M. Antonietti, *Angew. Chem. Int. Ed.*, 2005, **44**, 5576–5591.

4. W. T. S. Huck In *Nanoscale Assembly: Chemical Techniques* 2005, Springer, India.

5. K. J. Bishop, C. E. Wilmer, S. Soh and B.A. Grzybowski, *Small*, 2009, **5**, 1600–1630.

6. D. M. Vriezema, M. C. Aragones, J. A. A. W. Elemans, J. J. L. M. Cornelissen, A. E. Rowan and R. J. M. Nolte, *Chem. Rev.*,2005, **105***, 1445–1489.

7. H. Chen, J. He, C. Zhang and H. He, *J. Phys. Chem. C*, 2007, **111**, 18033–18038.

8. A. K. Sinha, M. Pradhan and T. Pal, *J. Phys. Chem. C*, 2013, **117**, 23976–23986.

9. Z. Chen, Z. Jiao, D. Pan, Z. Li, M. Wu, C. –H. Shek, C. M. L. Wu and J. K. L. Lai, *Chem. Rev.*, 2012, **112**, 3833–3855.

10. S. K. Bikkarolla, F. Yu, W. Zhou, P. Joseph, P. Cumpson and P. Papakonstantinou, *J. Mater. Chem. A*, 2014, **2**, 14493–14501.

11. L. Que, Jr. and W. B. Tolman, *Nature*, 2008, **455**, 333–340.

12. R. J. K. Taylor, M. Reid, J. Foot and S. A. Raw, *Acc. Chem. Res.*, 2005, **38**, 851–869.

13. S. L. Brock , N. Duan , Z. R. Tian, O. Giraldo, H. Zhou and S. L. Suib, *Chem. Mater.*, 1998, **10**, 2619–2628.

14. M. Amini, M. M. Najafpour, S. Nayeri, B. Pashaei and M. Bagherzadeh, *RSC Adv.*, 2012, **2**, 3654–3657.

15. S. K. Ghosh, J. Kang, M. Inokuchi and N. Toshima, *Appl. Catal. A*, 2013, **464**, 225–232.

16. I. Djerdj, D. Arčon, Z. Jagličić and M. Niederberger, *J. Phys. Chem. C*, 2007, **111**, 3614–3623.

17. P. Li, C. Nan, Z. Wei, J. Lu, Q. Peng and Y. Li, *Chem. Mater.*,2010, **22**, 4232–4236.

18. N. Birkner, S. Nayeri, B. Pashaei, M. M. Najafpour, W. H. Casey and A. Navrotsky, *Proc. Natl. Acad. Sci. USA*, 2013, **110**, 8801–8806.

19. A. Ramírez, P. Hillebrand, D. Stellmach, M. M. May, P. Bogdanoff and S. Fiechter, *J. Phys. Chem. C*, 2014, **118**, 14073–14081.

20. S. Yin, X. Wang, Z. Mou, Y. Wu, H. Huang, M. Zhu, Y Du and P. Yang, *Phys. Chem. Chem. Phys.*, 2014, **16**, 11289–11296.

21. S. Liu, Z. R. Tang, Y. Sun, J. C. Colmenares and Y. Xu, *Chem. Soc. Rev.*, 2015, **44**, 5053–5075.

22. N. Zhang, M. –Q. Yang, S. Liu, Y. Sun and Y. –J. Xu, *Chem. Rev.*, 2015, **115**, 10307–10377.

23. M. –Q. Yang, N. Zhang, M. Pagliaro and Y. –J. Xu, *Chem. Soc. Rev.,* 2014, **43**, 8240–8254.

24. P. V. Kamat, *J. Phys. Chem. Lett.*, 2012, **3**, 663−672.

25. S. K. Dutta, S. K. Mehetor and N. Pradhan *J. Phys. Chem. Lett.*, 2015, **6**, 936−944.

26. A. Fujishima and K. Honda, *Nature*, 1972, **238**, 37−40.

27. P. Zucca, C. Vinci, F. Sollai, A. Rescigno and E. Sanjust, *J. Mol. Catal. A*, 2008, **288**, 97–102.

28. M. Panizza and M. A. Oturan, *Electrochim. Acta*, 2011, **56**, 7084–7087.

29. L. Qifu, N. Guohua, J. Yiman, W. Wenwei and M. Yuedong, *Plasma Sci. Technol.*, 2014, **16** 1036–1041.

30. G. Liu, X. Li, J. Zhao, S. Horikoshi and H. Hidaka, *J. Mol. Catal.*, 2000, **153**, 221–229.

31. S Sood, S. K. Mehta, A. Umar and S. K. Kansal,*New J. Chem.*, 2014, **38**, 3127–3136.

32. S. K. Kansal, R. Lamba, S. K. Mehta and A. Umar, *Mater. Lett.*, 2013, **106**, 385–389.

33. S. Siva Kumar, V. Ranga Rao and G. Nageswara Rao, *Proc. Natl. Acad. Sci. India A*, 2013, **83**, 309–315.

34. B. N. Patil, D. B. Naik and V. S. Shrivastava, *Adv. Sci. Lett.*, 2011, **4**, 11–12.

35. V. Rodríguez-González, F. Paraguay-Delgado, X. García-Montelongo, L. M. Torres–Martínez and R. Gómez, *J. Ceramic Proc. Res.*, 2008, **9**, 606–610.

36. H. Lachheb, E. Puzenat, A. Houas, M. Ksibi, E. Elaloui, C. Guillard and J. –M. Herrmann, *Appl. Catal. B*, 2002, **39**, 75–90.

37. P. Tian, L. Sun, G. Liu, Y. H. Kang, J. D. Duan and W. L. Du, *Adv. Mater. Res.*, 2013, **643**, 170–173.

38. V. J. Babu, R. S. R. Bhayatharini and S. Ramakrishna, *RSC Adv.*, 2014, **4**, 19251–19256.

39. R. Vinu and G. Madras, *Environ. Sci. Technol.*, 2009, **43**, 473–479.

40. J. Wu, J. Cao, W. –Q. Han, A. Janotti and H. –C. Kim, In *Functional Metal Oxide Nanostructures*, Springer Series in Materials Science, 2012, Springer, New York.

41. Y. Yang, L. Zhu, X. Yang, E. Shao, X. Deng, N. Liu and M Wu, *J. Mater. Chem. A*, 2015, **3**, 2934–2941.

42. P. Zhang, Y. Zhan, C. C. Hao, J. Wang, C. Liu, Z. Meng, Z. Yin and W. Chen, *Nano Res.*, 2010, **3**, 235–243.

43. R. Tarik, P. Jean-Yves, S. Lorette, H. Frédéric, B. Emmanuel, B. Marc and A. Ahmed, *Appl. Catal. A*, 2010, **386**, 132–139.

44. H. Nishita, H. Hashimoto, N. Kimura, N. Miyata, T. Fuji, B. Ohtani and J. Takada, *RSC Adv.*, 2012, **2**, 6420–6423.

45. A. Khalid, A. Mohamed, Z. Qiumei, W. Kangbing and K. Huang, *J. Solid State Chem.*, 2010, **183**, 744–751.

46. N. Li, G. Zhenfeng, C. Minhua, R. Ling, Z. Xinyu, L. Bing, T. Yuan and C. Hu, *Carbon*, 2013, **54**, 124−132.

47. B. Zhongchao, S. Bo, F. Na, J. Zhicheng, L. Menghua, X. Liqiang and Q. Yitai, *Chem. Eur. J.*, 2012, **18**, 5319–5324.

48. M. A. Fox and M. T. Dulay, *Chem. Rev.*, 1993, **93**, 341-357.

49. S. K. Ghosh, M. Ali and H. Chatterjee, *Chem. Phys. Lett.*, 2013, **561–562**, 147–152.

50. W. S. Kijlstra, E. K. Poels, A. Bliek, B. M. Weckhuysen and R. A. Schoonheydt, *J. Phys. Chem. B*, 1997, **101**, 309–316.

51. A. Vázquez-Olmos, R. Redón, A. L. Fernández-Osorio and J. M. Saniger, *Appl. Phys. A*, 2005, **81**, 1131−1134.

52. S. Tsunekawa, T. Fukuda and A. Kasuya, *J. Appl. Phys.*, 2000, **87**, 1318−1321.

53. H. Rahaman, R. M. Laha, D. K. Maiti and S. K. Ghosh, *RSC Adv.*, 2015, **5**, 33923−33929.

54. A. Giri, N. Goswami, M. Pal, M. Tay, Z. Myint, S. Al-Harthi, A. Singha, B. Ghosh, J. Dutta and S. K. Pal, *J. Mater. Chem. C*, 2013, **1**, 1885–1895.

55. T. Ahmad, K. V. Ramanujachary, S. E. Lofland and A. K. Ganguli, *J. Mater. Chem.*, 2004, **14**, 3406–3410.

56. J. W. Lee, A. S. Hall, J. –D. Kim and T. E. Mallouk, *Chem. Mater.*, 2012, **24**, 1158−1164.

57. H. –P. Cong and S. −H. Yu, *Adv. Funct. Mater.*, 2007, **17**, 1814–1820.

58. A. Mehra and P. Venkateswarlu, *J. Chem. Phys.*, 1968, **48**, 4381–4383.

59. S. Xie, X. Zhou, X. Han, Q. Kuang, M. Jin, Y. Jiang, Z. Xie and L. Zheng, *J. Phys. Chem. C*, 2009, **113**, 19107–19111.

60. S. Brunauer, P. H. Emmett and E. Teller, *J. Am. Chem. Soc.*, 1938, **60**, 309–319.

61. S. K. Sahu, B, Huang, K. Lilova, B, F. Woodfield and A. Navrotsky, *Phys. Chem. Chem. Phys.,* 2015, **17**, 22286–22295.

62. N. Birkner and A. Navrotsky, *Proc. Natl. Acad. Sci. USA*, 2014, **111**, 6209–6214.

63. D. Su, H. –J. Ahn and G. Wang, *J. Mater. Chem. A*, 2013, **1**, 4845–4850.

64. A. Claro, M. J. Melo, S. Schäfer, J. S. S. de Melo, F. Pina, K. J. van den Berg and E. Aviva Burnstock, *Talanta* 2008, **74**, 922–929.

65. G. Liu, T. Wu, J. Zhao, H. Hidaka and N. Serpone, *Environ. Sci. Technol.*, 1999, **33**, 2081−2087.

66. C. Miliani, A. Romani and G. Favaro, *J. Phys. Org. Chem.,*2000, **13,** 141–150.

67. F. Polzer, S. Wunder, Y. Lu and M. Ballauff, *J. Catal.*, 2012, **289**, 80–87.

68. K. Laurier, F. Vermoortele, R. Ameloot, D. E. De Vos, J. Hofkens and M. Roeffaers, *J. Am. Chem. Soc*., 2013, **135**, 14488−14491.

69. G. Rothenberg, In *Advanced Synthesis and Catalysis*, Wiley-VHC, Weinheim, 2008.

70. M. Peplow, *Nature*, 2013, **495**, S10–S11.

71. S. Ghosh, S. Khamarui, K. S. Gayen and D. K. Maiti, *Sci. Rep.,* 2013, **3**, 2987 1-7.

72. M. Turner, V. B. Golovko, O. P. H. Vaughan, P. Abdulkin, A. Berenguer-Murcia, M. S. Tikhov, B. F. G. Johnson and R. M. Lambert, *Nature,* 2008, **454**, 981–984.

73. K. S. Gayen, T. Sengupta, Y. Saima, A. Das, D. K. Maiti and A. Mitra, *Green Chem.*, 2012, **14**, 1589–1592.

74. V. Polshettiwar, J. −M. Basset and D. Astruc, *ChemSusChem.,* 2012, **5**, 6–8.

75. B. C. Ranu, D. Saha, D. Kundu and N. Mukherjee, In *Nanocatalysis: Synthesis and Applications* of *Aryl Carbon-Heteroatom Coupling Reactions using Nano-Metal Catalyst*, V. Polshettiwar, T. Asefa eds. Wiley–VCH, Weinheim, 2013.

76. R. S. Varma, *Sustainable Chemical Processes*, 2014, **2,** 11 1–8.

77. Z. Chen, Z. Jiao, D. Pan, Z. Li, M. Wu, C. –H. Shek, C. M. L. Wu and K. L. L. Joseph, *Chem. Rev.,* 2012, **112**, 3833–3855.

78. W. Weifeng, C. Xinwei, C. Weixing and G. I. Douglas, *Chem. Soc. Rev.,* 2011, **40**, 1697–1721.

79. G. S. Thomas, J. R. Bargar, S. Garrison and M. T. Bradley, *Acc. Chem. Res.,* 2010, **43**, 2–9.

80. V. Polshettiwar, B. Baruwati and R. S. Varma, *ACS Nano,* 2009, **3**, 728–736.

81. Z. Hao, C. Gaoping, W. Zhiyong, Y. Yusheng, S. Zujin and G. Zhennan, *Nano Lett.,* 2008, **8**, 2664–2668.

82. Y. Hirao, C. Yokoyama and M. Makoto, *Chem. Commun.,* 1996, 597–598.

83. E. A. Kotomin, Y. A. Mastrikov, E. Heifets and J. Maier, *Phys. Chem. Chem. Phys*., 2008, *10*, 4644–4649.

84. Z. W. Chen, S. Y. Zhang, S. Tan, J. Wang and S. Z. Jin, *Appl. Phys. A*, 2004, **78**, 581–584.

85. S. Huang, Y. Ding, Y. Liu, L. Su, R. Filosa Jr. And Y. Lei, *Electroanalysis*, 2001, **23**, 1912–1920.

86. J. –H. Kim, K. H. Lee, L. J. Overzet and G. S. Lee, *Nano Lett*., 2011, **11**, 2611–2617.

87. M. M. Thackeray, C. S. Johnson, J. T. Vaughey, N. Li and S. A. Hackney, *J. Mater. Chem.*, 2005, **15**, 2257–2267.

88. O. Giraldo, S. L. Brock, W. S. Willis, M. Marquez and S. L. Suib, *J. Am. Chem. Soc.,* 2000, **122**, 9330–9331.

89. S. K. Nayak and P. Jena, *Phys. Rev. Lett.*, 1998, **81**, 2970–2973.

90. E. Lidstrom, O. Hartmann, *J. Phys: Condens. Matter.,* 2000, *12*, 4969–4974.

91. J. E. Pask, D. J. Singh, I. I. Mazin, C. S. Hellberg and J. Kortus, *Phys. Rev. B,* 2001, **64**, 024403 1–3.

92. I. Djerdj, D. Arčon, Z. Jagličić and M. Niederberger, *J. Phys. Chem. C,* 2007, **111**, 3614–3623.

93. R. Ma, Y. Bando, L. Zhang and T. Sasaki, *Adv. Mater.,* 2004, **16**, 918–922.

94. F. Y. Cheng, J. A. Shen, B. Peng, Y. D. Pan and Z. L. Tao, *J. Chen, Nature Chem.,* 2011, **3**, 79–84.

95. Y. Oaki and H. Imai, *Angew. Chem. Int. Ed.,* 2007, **119**, 5039–5043.

96. H.M. Zang and Y. Teraoka*, Catal. Today,* 1989, **6**, 155–162.

97. B. Ammundsen and J. Paulsen, *Adv. Mater.,* 2001, **13**, 943–956.

98. Y. F. Chang and J. C. McCarty, *Catal. Today,* 1996, **30**, 163–170.

99. P. Serp, K. Philippot, G. A. Somorjai and B. Chaudret, In *Nanomaterials in Catalysis,* Wiley-VCH, Winheim, 2013.

100. L. Hu, Q. Peng and Y. Li, *J. Am. Chem. Soc.*, 2008, **130**, 16136–16137.

101. A. Tokeer, K. V. Ramanujachary, S. E. Lofland and G. Ashok, *J. Mater. Chem.*, 2004, **14**, 3406–3410.

102. Y. –F. Han, F. Chen, Z. Zhong, K. Ramesh, L. Chen and E. Widjaja, *J. Phys. Chem. B*, 2006, **110**, 24450–24456.

103. C. Hongmin and H. Junhui, *J. Phys. Chem. C,* 2008, **112**, 17540–17545.

104. S. Gnanam and V. Rajendran, *J. Sol-Gel Sci. Technol.,* 2011, **58**, 62–69.

105. L. Liu, H. Liang, H. Yang, J. Wei and Y. Yanzhao, *Nanotechnology,* 2011, **22**, 015603–015611.

106. Y. Qiu, G. –L. Xu, K. Yan, H. Sun, J. Xiao, S. Yang, S. –G. Sun, L. Jin and H. Deng, *J. Mater. Chem.*, 2011, **21**, 6346–6353.

107. J. Cao, Q. Mao and Y. Qian, *J. Solid State Chem.,* 2012, **191**, 10–14.

108. M. Amini, M. M. Najafpour, S. Nayeri, B. Pashaei and M. Bagherzadeh, *Dalton Trans.*, 2012, **41**, 11026–11031.

109. T. Mallat and A. Baiker, *Chem. Rev.,* 2004, **104**, 3037–3058.

110. C. J. Weiss, P. Das, D. L. Miller, M. L. Helm and A. M. Appel, *ACS Catal.,* 2014, **4**, 2951–2958.

111. D. Könning, T. Olbrisch, F. D. Sypaseuth, C. C. Tzschucke and M. Christmann, *Chem. Commun.*, 2014, **50**, 5014–5016.

112. Y. Hong, X. Yan, X. Liao, R. Li, S. Xu, L. Xiao and J. Fan, *Chem. Commun.,* 2014, **50**, 9679–9682.

113. Z. -A. Qiao, P. Zhang, S. –H. Chai, M. Chi, G. M. Veith, N. C. Gallego, M. Kidder and S. Dai, *J. Am. Chem. Soc.,* 2014, **136**, 11260–11263.

114. D. K. Maiti, N. Chatterjee, P. Pandit and S. K. Hota, *Chem. Commun.* 2010, **46**, 2022–2024.

115. S. Khamarui, R. Maiti and D. K. Maiti, *Chem. Commun.,* 2015, **51**, 384–387.

116. Q. Javed, F. –P. Wang, M. Y. Rafique, A. M. Toufiq and M. Z. Iqbal, *Chinese Phys. B*, 2012, **21**, 117311 1–7.

117. Y. Li, H. Tan, O. Lebedev, J. Verbeeck, E. Biermans, G. van Tendeloo and B. –L. Su, *Cryst. Growth Des.*, 2010, **10**, 2969–2976.

118. G. Yang, W. Yan, J. Wang and H. Yang, *Cryst. Eng. Comm.,* 2014, **16**, 6907–6913.

119. L. Ling, L. Hui, Y. Hongxiao, W. Jingjing and Y. Yanzhao, *Nanotechnology,* 2011, **22**, 015603–015611.

120. S. K. Ghosh, M. Ali and H. Chatterjee, *Chem. Phys. Lett.,* 2013, **561**, 147–152.

121. C. M. Julien, M. Massot and C. Poinsignon, *Spectrochim. Acta A,* 2004, **60**, 689–700.

122. Y. T. Chua, P. C. Stair and I. E. Wachs, *J. Phys. Chem. B*, 2001, **105**, 8600–8606.

123. F. Buciuman, F. Patcas, R. Cracium and D. R. T. Zahn, *Phys. Chem. Chem. Phys*., 1999, **1**, 185–190.

124. Y. Luo, Y. –Q. Deng, W. Mao, X. –J. Yang, K. Zhu, J. Xu and Y.-F. Han, *J. Phys. Chem. C,* 2012, **116**, 20975–20981.

125. Y. F. Chang and J. C. McCarty, *Catal. Today,* 1996, **30**, 163−170.

126. S. Brunauer, P. H. Emmett and E. Teller, *J. Am. Chem. Soc.*, 1938, **60**, 309–319.

127. M. Uyanik and K. Ishihara, *Chem. Commun.,* 2009, 2086–2099.

128. J. Zhu, K. Kailasam, A. Fischer and A. Thomas, *ACS Catal*., 2011, **1**, 342–347.

129. H. Caot and S. L. Suib, *J. Am. Chem. Soc.,* 1994,**116**, 5334–5342.

130. X. Fu, J. Feng, H. Wang and K. M. Ng, *Nanotechnology,* 2009, **20**, 375601–375610.

131. J. Chen, J. C. Lin, V. Purohit, M. B. Cutlip and S. L. Suib *Catal. Today*, 1997, **33**, 205–214.